Title: Strong dispersion effect of cobalt spinel active phase spread over ceria for catalytic N_2O decomposition: the role of the interface periphery

Author: G. Grzybek P. Stelmachowski S. Gudyka P. Indyka Z. Sojka N. Guillén-Hurtado V. Rico-Pérez A. Bueno-López A. Kotarba

PII: S0926-3373(15)30046-1
DOI: http://dx.doi.org/doi:10.1016/j.apcatb.2015.07.027
Reference: APCATB 14171

To appear in: *Applied Catalysis B: Environmental*

Received date: 8-5-2015
Revised date: 10-7-2015
Accepted date: 18-7-2015

Please cite this article as: G.Grzybek, P.Stelmachowski, S.Gudyka, P.Indyka, Z.Sojka, N.Guillén-Hurtado, V.Rico-Pérez, A.Bueno-López, A.Kotarba, Strong dispersion effect of cobalt spinel active phase spread over ceria for catalytic N2O decomposition: the role of the interface periphery, Applied Catalysis B, Environmental http://dx.doi.org/10.1016/j.apcatb.2015.07.027

Strong dispersion effect of cobalt spinel active phase spread over ceria for catalytic N_2O decomposition: the role of the interface periphery

G. Grzybek[a*], P. Stelmachowski[a], S. Gudyka[a], P. Indyka[a], Z. Sojka[a], N. Guillén-Hurtado[b], V. Rico-Pérez[b], A. Bueno-López[b], A. Kotarba[a]

[a] Faculty of Chemistry, Jagiellonian University, Ingardena 3, 30-060 Krakow, Poland

[b] Department of Inorganic Chemistry, University of Alicante, Ap.99, E-03080 Alicante, Spain

*Corresponding author: Faculty of Chemistry, Jagiellonian University, ul. Ingardena 3, 30-Highlights

060 Krakow, Poland, Fax No. +48 12 6340515, Phone No. +48 12 6632246, e-mail: maniak@chemia.uj.edu.pl

Highlights

10 wt.% of Co_3O_4/CeO_2 reproduces the activity of bare Co_3O_4 catalyst

The highest apparent reaction rate is observed for the 1 wt.% of Co_3O_4

Strong dispersion effect is associated with morphology of Co_3O_4/CeO_2 system

Co_3O_4/CeO_2 interface length accounts for the observed specific activity in deN_2O

Abstract

A series of Co_3O_4/CeO_2 catalysts with increasing cobalt spinel loading in the range of 1-20 wt.% was prepared by incipient wetness impregnation of CeO_2. The obtained catalysts were thoroughly examined by XRD, XPS, XRF, RS, TEM/EDX/EELS, TPR and BET techniques. The catalytic tests in deN_2O reaction revealed that the 10 wt.% of cobalt spinel in supported system is able to reproduce the activity of bare Co_3O_4 catalyst. However, it was found that the catalyst with the lowest content of Co_3O_4 equal to 1 wt.% exhibits the highest apparent reaction rate per mass of the spinel active phase. The observed activity was explained basing

on the transmission electron microscopy analysis in terms of the dispersion of spinel phase over ceria support. A simple model that accounts for the observed strong dispersion effect is proposed. It consists in a two-step mechanism, where N_2O is dissociated on the spinel nanograins and the resultant oxygen species are preferentially recombined at the Co_3O_4/CeO_2 interface periphery.

Keywords

cobalt spinel; CeO_2; N_2O decomposition; supported catalyst; oxygen spillover

1. Introduction

Nitrous oxide has been recognized as one of the most important greenhouse gases with a lifetime of 150 years in the atmosphere, and the global warming potential 310 times higher than that of CO_2 [1]. Moreover, N_2O contributes to destruction of the ozone layer in the stratosphere. For these reasons, decomposition of N_2O into N_2 and O_2 is a subject of continuous intensive investigations [2]. Taking into account the high temperature of thermal decomposition of nitrous oxide, over 650 ºC, catalytic decomposition of N_2O is considered as an economically driven solution practical for practical applications.

Among the anthropogenic sources of nitrous oxide, adipic and nitric acid plants dominate [3]. In the case of the former, due to high concentration of N_2O in the tail gases and the exothermal effect of its decomposition, operational abatement system has been already developed [3,4]. On the contrary, the low concentration of the pollutant and presence of inhibiting co-reactants (H_2O, O_2 and NO_x) in the residual gases of the nitric acid plant results in still persistent searching for efficient low-cost catalyst for low temperature conditions (below 400°C).

Up to now, many catalytic systems such as noble metals [5,6,7], metal oxides [8,9,10], ion-exchanged zeolites, calcined hydrotalcites [[11,12,13], mesoporous silicas [14,15] were investigated for the low temperature deN_2O reaction. One of the simple promising generic systems exhibiting high catalytic activity in this reaction is cobalt spinel [16,17,18,19,20], which can be additionally modified by structural [21,22,23,24] and surface donation [24,25,26,27,28]. The N_2O decomposition over cobalt spinel is a classic redox reaction, involving N_2O molecule activation by electron transfer from cobalt(II) cation to N_2O

molecule (Equation 1), oxygen species diffusion and finally their recombination into O_2 molecule (Equation 2), closing the catalytic cycle:

$$N_2O + e^- \rightarrow N_2^{\uparrow} + O^- \quad (1)$$

$$2\ O^- \rightarrow O_2^{\uparrow} + 2\ e^- \quad (2)$$

Alternatively, dioxygen may also be produced in a non-diffusive pathway via Eley-Ridel mechanism:

$$O^- + N_2O \rightarrow O_2^{\uparrow} + N_2^{\uparrow} \quad (3)$$

Despite the promising reactivity in deN_2O reaction, preparation of final catalyst based on Co_3O_4 as a bulk oxide active phase cannot be taken into account due to the high price of cobalt. However, for practical applications this problem can be easily solved by dispersion of cobalt spinel active phase on a high surface area support such as alumina, silica, magnesia or ceria [29,30,31,32,33,34,35]. Among them CeO_2, owing to its particular properties (redox and oxygen storage capacity), in many cases appeared to be superior for deN_2O catalytic application [36]. Although ceria was quite frequently used as a carrier of noble metals for nitrous oxide decomposition, it is less used to support redox oxides of transition metals.

The aim of this study was to investigate a supported Co_3O_4/CeO_2 catalyst of high deN_2O activity, in order to understand the mechanistic role of active phase/support periphery. To achieve this goal a series of catalysts was prepared by dispersion of nanocrystalline Co_3O_4 on the surface of CeO_2 support with various Co loadings and tested in the N_2O decomposition. Thorough characterization by means of XRD, XPS, XRF, RS, TEM/EDX/EELS, TPR and BET allowed to propose a simple topological model of the catalyst for interpretation of the observed reactivity trends.

2. Experimental

2.1. Catalysts preparation

The ceria support was prepared from $Ce(NO_3)_3 \cdot 6H_2O$ (Sigma Aldrich, 99,99%) by calcination at 500°C for 4 h. Cobalt spinel was loaded on CeO_2 by incipient wetness impregnation of CeO_2 with water solution of $Co(NO_3)_2 \cdot 6H_2O$ (Sigma Aldrich, 98%) with the appropriate concentrations to obtain a cobalt spinel content of 1, 5, 7.5, 10 and 20 wt.% for series. The samples were next dried at 100°C for 12 h, and calcined in air at 400°C for 4 h. Before deN_2O activity tests the catalysts were activated *in situ* in gas flow by temperature-programed heating

till 600^{o}C monitoring simultaneously the removal of the adsorbed impurity gases, such as H_2O and CO_2 by mass spectrometer.

2.2. Catalysts characterization

Relative bulk content of cobalt and cerium oxides in the investigated catalysts (in form of pellets, 10 mm in diameter) was determined with the use of Energy-Dispersive XRF spectrometer (Thermo Scientific, ARL QUANT'X). The X-rays of 4-50 kV (1 kV step) with the beam size of 1 mm were generated with the Rh anode. The detector used was a 3.5 mm Si(Li) drifted crystal with a Peltier cooling (~ 185 K). For quantitative analysis, the calibration with a series of metallic standards and an UniQuant software were used.

X-ray diffractograms were recorded in a Bruker D8-advance diffractometer, using CuKα radiation (λ= 1.540598 Å). Diffractograms were recorded for 2θ in the range of 10° - 80° with a step of 0.02°, and a time of 3 s per step. The BET surface area of the catalysts determined by N_2 adsorption at −196 °C in an automatic volumetric system (Autosorb-6, Quantachrome) showed no significant changes in the surface area upon cobalt spinel loading (65 − 80 m^2/g).

The Raman spectra recorded at room temperature in ambient conditions were taken using a Renishaw InVia spectrometer equipped with a Leica DMLM confocal microscope and a CCD detector with an excitation wavelength of 785 nm. The Raman scattered light was collected in the spectral range of 100 - 800 cm^{-1} with a resolution of 1 cm^{-1}. At least five scans were accumulated to ensure a sufficient signal to noise ratio.

Temperature programmed reduction by H_2 of the catalysts was carried out in a Micromeritics Pulse ChemiSorb 2705 device with a thermal conductivity detector (TCD). The tests were performed in a tubular quartz reactor in the range of 20–1050°C (10 °C/min) with the use of 20 mg of fresh catalyst, and the flow rate of the feed (5 % H_2 in Ar) of 40 ml/min. Water was removed by a cold trap (−89 ºC) placed before the TCD.

The X-ray photoelectron spectra (XPS) were measured with a Prevac spectrometer equipped with a hemispherical VG SCIENTA R3000 analyzer. The spectra were recorded using a monochromatized AlKα source (E = 1486.6 eV), and an electron flood gun (FS40A-PS) to compensate the residual charge on the surface. Before spectra acquisition the samples were outgassed at c.a. 50°C for at least 15 min, and the background pressure in the chamber during the measurements was 5×10^{-9} mbar. The spectra were recorded with a pass energy of 100 eV for the survey and narrow scans. All the binding energies were referenced to the C 1s

peak at 285 eV of the adventitious carbon. The Tougaard-Shirley and linear type baselines implemented in CasaXPS software were applied prior the analysis of the area of the photo-peaks and estimation of the integration error. The surface composition of the samples was determined by analysis of the Co 2p, Ce 3d and O 1s photoelectron peaks areas.

The Co_3O_4/CeO_2 catalysts (1, 5, 10 wt. % loading) were investigated by means of high resolution analytical transmission electron microscopy (FEI Tecnai Osiris) with X-FEG Schottky field emitter operated at accelerating voltage of 200 kV. The samples were dispersed in ethanol, ultrasonicated (20kHz, 200W, 5min), dropped into a lacey carbon-coated copper grid, and dried at room temperature. The samples were loaded into a beryllium double-tilt low-background holder in order to reduce the production of spurious X-rays. TEM images were recorded by a Gatan CCD camera in a digital format. A Fischione High Angle Annular Dark Field (HAADF) detector for Z contrast imaging was used in the scanning transmission electron microscopy (STEM) mode. Super-X windowless EDX (Energy Dispersive X-ray) detector system with silicon drift detector (SDD) was used for elemental mapping. STEM images coupled with EDX elemental mapping were acquired with applied sample drift correction (Bruker Esprit software). The EELS spectroscopy measurements were acquired on a GIF-Quantum spectrometer (with about 1.0 eV energy resolution) using spectrum imaging technique (SI). The spatial resolution of the chemical information gathered by EELS was kept below 1 nm.

2.3. N_2O decomposition tests

The N_2O decomposition tests were performed in two modes: isothermal and with a steady temperature ramp. The isothermal tests were carried out at steady-state conditions in the range of 200-600 °C with the heating step of 25 °C, at atmospheric pressure in a 10 mm i.d. cylindrical fixed-bed reactor, with 50 mg of the catalyst and a total gas flow of 50 ml/min (GHSV = 30’000 h^{-1}). The catalytic bed was packed between plugs of quartz wool. The 1000 ppm N_2O/He mixture was used. The gas composition was analyzed by a HP 6890 gas chromatograph equipped with a thermal conductivity detector and two serial columns (Porapak Q, for N_2O, and Molecular Sieve 13X, for O_2 and N_2). Tests with a steady temperature ramp, temperature-programmed catalytic reaction, were performed in a quartz flow reactor in the range of 20–600°C (10 °C/min) with the use of 300 mg of the catalyst (sieve fraction of 0.2–0.3 mm), flow rate of the feed (5% N_2O in Ar) of 7’000 h^{-1}. The

reaction progress was monitored with a quadrupole mass spectrometer (RGA200, SRS, lines for m/z = 44, 32, 28, 30 and 18, corresponding to N_2O, O_2, NO, N_2 and H_2O).

To check the catalyst stability catalytic tests were always performed at least in two consecutive runs. In all cases the results were fully reproducible within the experimental error. It is worth mentioning that this crucial issue was already investigated at both laboratory and pilot plant scales, as describes in our previous papers [24,37]. The results of the studies confirmed that no appreciable deterioration of the catalyst performance takes place for more than 1600 h time on steam.

3. Results and Discussion

3.1. Elemental and structural characterization

Elemental composition analysis of the investigated samples is summarized in Table 1. The bulk content of Co_3O_4 phase, based on XRF analysis, reflects the desired cobalt phase loading. The surface composition is discussed in the XPS section. The crystalline structure of the prepared catalysts was studied by XRD and Raman spectroscopy. The X-ray diffraction patterns of the bare ceria support and supported cobalt spinel catalysts are shown in Figure 1. The most intense diffraction line at a 2θ value of 28.6° corresponds to the (111) plane of the cubic ceria oxide phase (ICSD – 28753). The diffraction lines at 2θ values of 33.2°, 47.5° and 56.4° are assigned to (200), (220) and (311) reflections of CeO_2, respectively. All of the diffraction peaks of cerium(IV) oxide are observed in supported cobalt catalysts, as well. The presence of cobalt spinel for the samples with the loading of 10 and 20 wt.% is manifested by peaks at 2θ value of 36.8°, 44.8° and 65.5° due to (311), (400) and (440) reflections of Co_3O_4 phase, respectively (69378-ICSD). The absence of the diffraction peaks of the cobalt spinel samples with the content lower than 10 wt.% is caused by the small particles size of Co_3O_4 dispersed on the ceria surface as reported in [38,39], but their presence was confirmed by the TEM and Raman results (see below). The XRD results were supported by the Raman spectroscopy characterization. The Raman spectrum of the ceria support, presented in Figure 2, shows a characteristic single, broad and intense band located at 465 cm^{-1}. This peak is assigned to the F_{2g} phonon mode of cubic fluorite CeO_2 [40,41]. This band was also detected in the Raman spectra for the ceria-supported cobalt spinel catalysts with the Co_3O_4 content in the whole range of 1-20 wt.%. Additionally, in the spectra of the ceria-supported cobalt catalysts (5-20 %wt.) five active Raman modes typical of the spinel structure located at 196,

482, 522, 619 and 691 cm^{-1}, were observed, confirming the presence of nanocrystaline Co_3O_4 [42,43,44]. The position of the F_{2g} peak of the ceria support does not change upon deposition of the cobalt oxide phase regardless the Co loading, implying that cobalt do not form a solid solution with ceria, in contrast to previous claims [45]. Furthermore, it can be seen that introducing cobalt oxide results in a strong decrease of the CeO_2 support peak intensity, which may be caused by dispersion of cobalt oxide over the support and its higher absorption coefficient.

3.2. Catalysts characterization by H_2-TPR

The reducibility of CeO_2, 1% Co_3O_4/CeO_2, 10% Co_3O_4/CeO_2 and Co_3O_4, studied by H_2-TPR is presented in Figure 3. The TPR profile of pure CeO_2 shows two broad peaks centered at 550°C and 850 °C. They have been ascribed to the reduction of the surface and bulk Ce^{4+} ions to Ce^{3+}, respectively [46]. Deposition of cobalt spinel on the ceria surface leaves the bulk reduction peak of ceria intact, whereas the surface reduction is broadened and gradually disappears. The ceria carrier exhibits even stronger effect on the reducibility of the supported Co_3O_4 particles. The two overlapping peaks observed for bulk spinel, due to reduction of Co^{3+} ions to Co^{2+} (below 350 °C) and Co^{2+} ions to metallic Co (above 350 °C) [27,47] become better resolved and systematically shifted toward lower temperatures (Equations 4 and 5).

$$Co^{2+}Co^{3+}{}_2O_4 + H_2 \rightarrow 3Co^{2+}O + H_2O \qquad (4)$$

$$Co^{2+}O + H_2 \rightarrow Co^0 + H_2O \qquad (5)$$

This indicates that ceria is acting not only as a mere carrier but interacting strongly with the deposited spinel changing substantially the redox properties of both the active phase and the support. Since this shift increases with the cobalt spinel dispersion (see the microscopic observations section) it can be assumed that the observed redox changes are due to the interaction at the periphery of the Co_3O_4/CeO_2 interface.

3.3. Spectroscopic XPS characterization

The ceria support together with the Co_3O_4/CeO_2 catalysts with 1, 5, 10 and 20 wt. % Co_3O_4 loadings were investigated by XPS spectroscopy. The XPS spectra of Co 2p, Ce 3d and O 1s regions are shown in Figure 4, Figure 5 and Figure 6, respectively. The relative amount of Co and Ce are summarized in Table 1. The XPS and XRF results differ with regard to the

cobalt content because the both methods probe different sample regions. Whereas XPS collects electrons emitted from about 2, 3 top crystal layers of the unsheaded surface grains, the XRF which is based on the X-ray photons measurements penetrates the sample on a micrometric scale. In other words, a low escape depth of photoelectrons in contrast to the long escape depth of X-radiation result in different concentrations of the components obtained from the two methods, if the sample is inherently heterogeneous, which is the case of the cobalt spinel supported over ceria. Moreover, the XPS based results are more strongly dependent on the material morphology than those obtained from XRF. The larger the agglomeration of the cobalt particles the less are probed by surface sensitive XPS. These results, in fact, point out that the ceria support is non-uniformly covered by the Co_3O_4 particles in the case of the higher loadings, which is in line with the TEM observations.

For the Co_3O_4/CeO_2 samples the Co $2p_{3/2}$ and $2p_{1/2}$ lines appeared at 780 and 795 eV. The shape and the position of the observed lines are typical for cobalt spinel structure. With the increasing cobalt loading, the position of the main Co $2p_{3/2}$ peak is shifted towards lower BE, from 780.6 eV for 1% Co_3O_4 to 780.3, 780.1 and 779.7 eV for 5%, 10% and 20%, respectively. The energy shift is brought about by the changing in the relative content of Co^{2+} and Co^{3+} ions. At lower concentrations, due to a stronger interaction with ceria, the relative abundance of Co^{2+} with a 2p photopeak at higher BE is increased. Also, slightly smaller Co_3O_4 crystals, observed in TEM for lower loadings, may result in a change of local surface Madelung energy of cobalt ions resulting in the observed binding energy changes. The main Co 2p photopeak is often analyzed in terms of components arising from tetrahedral Co^{2+} and octahedral Co^{3+} [48]. The band at 779.2–779.6 eV is characteristic for Co^{3+} and that at 780.3–780.7 eV for Co^{2+}. The low quality of the Co 2p spectra, despite the long data acquisition during XP analysis, renders it impossible to decompose the peak in order to quantitatively compare Co^{3+} and Co^{2+} components for the series of the catalysts.

The O 1s spectra of CeO_2 reveal two main peaks, as shown in Figure 5. The peak at 529.3 eV is assigned to the lattice O^{2-} oxygen ions, while the second, less intense peak above 531 eV is usually assigned to surface hydroxyl groups, carbonates/adsorbed CO_2, etc. [49]. The position of the lattice oxygen peak does not change upon addition of different amounts of the Co_3O_4 phase. This is not surprising, since the O 1s peak for Co_3O_4 is expected around 529.7 eV [50].

The Ce 3d XPS spectra of Co_3O_4/CeO_2 samples consist of several overlapping peaks (Figure 6). Their positions and assignment are summarized in Table 2. Those denoted by v, v”, v”’

and u, u", u"' are attributed to the Ce^{4+} state, while those denoted by v^0 (usually poorly resolved), v' and u, u' are assigned to the Ce^{3+} state [49]. Since the Scoffield coefficient, σ, escape depth, λ, and other instrumental parameters, $S(E_{kin})$ are virtually the same for Ce^{3+} and Ce^{4+} states, the ratio of cumulative areas, I, due to bands assigned to Ce^{3+} and Ce^{4+} is practically equal the surface concentration ratio x_{Ce3+}/x_{Ce4+} as implied by Equation 6:

$$\frac{I_{Ce^{3+}}}{I_{Ce^{4+}}} = \frac{\sigma_{Ce^{3+}}(h\nu)S\left(E_{kin,Ce^{3+}}\right)\lambda_{Ce^{3+}}\left(E_{kin,Ce^{3+}}\right)x_{Ce^{3+}}}{\sigma_{Ce^{4+}}(h\nu)S\left(E_{kin,Ce^{4+}}\right)\lambda_{Ce^{4+}}\left(E_{kin,Ce^{4+}}\right)x_{Ce^{4+}}} = \frac{x_{Ce^{3+}}}{x_{Ce^{4+}}} \qquad (6)$$

The presence of Ce^{3+} is observed even for the support reference sample, without the Co_3O_4, and in all cases it can be accounted for by the oxygen release upon heat treatment of the catalysts [49]. It should be noted, however, that the relative amount of Ce^{3+} increases with the content of cobalt spinel loading (Table 1), in line with the TPR results. The XPS derived atomic Co/Ce ratio for the investigated catalysts differs from that obtained from the bulk XRF analysis, indicating much lower quantities of cobalt at the surface. Apparently, this effect is of general nature as it is observed for cobalt oxide supported on ceria [51] and ceria supported on cobalt oxide as well [52].

3.4. Morphological characterization by TEM microscopy

HAADF STEM images coupled with EDX maps of the Co_3O_4/CeO_2 catalysts presented in Figure 7a-c provide an overview of the typical morphological and chemical features of the examined samples with the Co_3O_4 loading of 1, 5 and 10 wt. %. Each sample exhibited 5-30 nm individual CeO_2 particles of elongated shape epitomized in the Figure 7a'-c' as nano-fibers (marked in orange), most often forming dispersed and loosely-bound particle aggregates. In turn, cobalt spinel particles exhibit a round shape (marked in red). In the case of 1 wt.% load sample ultrafine Co_3O_4 essentially isolated particles of the size below 10 nm can be distinguished, decorating ceria support (Figure 7a, a'). As the cobalt loading increases the individual spinel particles agglomerate forming larger patches (marked in red envelopes in Figure 7b'-c') of the averaged size of 20-50 nm and 50-100 nm for 5 and 10 wt. % Co_3O_4 loading, respectively. In the corresponding HRTEM image (Figure 7d, d') it is revealed that the spinel agglomerates are formed by individual nanocrystals of rombicubooctahedral shape described previously in detail in [53]. The appearance of lattice fringes indicates a crystalline character of both the ceria support and cobalt spinel active phase. The FFT patterns of the Co_3O_4/CeO_2 catalysts were projected by formula units of the cubic crystal structure along different crystallographic directions, as exemplified in Figure 7d-insert. Several exposed

facets of the CeO_2 can be identified as the (111) and (200) crystal planes with 0.31 nm and 0.27 nm lattice spacing, indexed along the [011] zone axis. For Co_3O_4 the interplanar distance of HRTEM fringes were identified as 0.47 nm and 0.28 nm, which agreed well with the d-value of the (111) and (110) crystal planes of cobalt spinel. The EELS chemical composition map [54], acquired from the mixed particles area with nanometer spatial resolution (Figure 7d'-insert) clearly shows the presence of the individual elemental contrast, which in combination with HRTEM images reveals the Co_3O_4-CeO_2 periphery in the nanoscale. Summarizing, in the case Co_3O_4 loading of 1% wt. the spinel active phase is present as isolated nanocrystal of 5-30 nm, whereas for increased loading they agglomerate into patches of 20-50 nm and 50-100 nm for 5 and 10 wt. % Co_3O_4, respectively. As a result the periphery between the active spinel phase and the ceria support is dramatically decreased calculated per cobalt loading (vide infra).

3.5. N_2O decomposition tests

Typical N_2O decomposition results for ceria supported Co_3O_4 catalysts are shown in Figure 8, where the experimental data are expressed as N_2O conversion (X_{N2O}) as a function of temperature. In order to analyze the effect of the cobalt spinel loading on the catalytic activity, the conversion and the apparent reaction rate ($\mu mol_{N2O} \cdot g_{Co3O4}^{-1} \cdot s^{-1}$) at 400°C for the series of Co_3O_4/CeO_2 catalysts were calculated (Table 3). The results clearly show that the catalytic activity of the material increases substantially with the loading of the cobalt spinel (Figure 9, blue line, conversion). It may be noticed that the most active sample, 10 wt.% Co_3O_4/CeO_2, with the conversion equal to 43% at 400°C, corresponds to the activity of the reference bulk cobalt spinel. However, the apparent reaction rate normalized to the spinel content derived from XRF for the series of samples increases dramatically with at low Co_3O_4 loadings (Figure 9, green line, r_{XRF}). This effect persist even in the case when reactivity data are normalized not to total (XRF) but to the surface cobalt concentration obtained from XPS data (Figure 9, black line, r_{XPS}).

These results imply that apart from the cobalt loading there is also a morphological factor associated with the different dispersion of the spinel active phase over the ceria, depending on the cobalt content (see Figure 7). Indeed, following the recent suggestions [35] we may assume that for the N_2O decomposition a well-developed interface between Co_3O_4 and CeO_2 plays a beneficial role. We may thus propose that the two-step mechanism of deN_2O operates

preferably at two topographically different sites. The first step of N_2O dissociation occurs on the spinel component, whereas the second step of recombination of the resultant oxygen species proceeds at higher turnover at the periphery of the Co_3O_4 grains/agglomerates on the CeO_2 surface. The involvement of the ceria support is implied by the dependence of the N_2O conversion on the ceria reduction degree (Figure 10, where X_{N2O} at 400°C is plotted against Ce^{3+} fraction). The extent of interaction of the cobalt phase with the ceria support can be followed by the relative amount of the cerium in the reduced state, based on the XPS measurements (Table 1). With the increasing cobalt loading, the amount of the Ce^{3+} ions increases, indicating again the importance of the Co_3O_4/CeO_2 interface area, at least in an indirect way.

In order to account for the observed trends of specific activity of the dispersed cobalt spinel phase (r_{XRF}, r_{XPS}) two simple geometrical models of the Co_3O_4/CeO_2 interface were tested. Basing on the TEM observations, at the first approximation we may approximate the Co_3O_4 spinel nanometric domains as hemispherical or cylindrical in shape. These geometrical models were then used to validate the assumption that the specific reaction rate, r_{peri}, is proportional to the extent of the Co_3O_4/CeO_2 interface periphery. As revealed by the TEM analysis for 1 wt.% Co_3O_4 loading, the cobalt spinel nanoparticles are in the size of about 10 nm, while for higher loadings, the Co_3O_4 crystallites agglomerate into the compact domains with the average sizes of ~35 nm and ~75 nm for 5 and 10 wt.% Co_3O_4, respectively. The periphery of such domains may be then used for regularization of the observed r_{XRF} values in terms of reaction rate express as number of N_2O molecules (μmol_{N2O}) decomposed per unit periphery length (nm^{-1}), thus the ultimate specific rate of deN_2O decomposition was calculated ($r_{peri}/\mu mol_{N2O}\cdot s^{-1}\cdot nm^{-1}$). In case of the cylindrical model all of the calculated specific reaction rates were in the narrow range of 0.8 – 0.9 $\mu mol_{N2O}\cdot s^{-1}\cdot nm^{-1}$ (Figure 9, red line, r_{peri}). For the semi-spherical model the reaction rate varied from 0.27 $\mu mol_{N2O}\cdot s^{-1}\cdot nm^{-1}$ for 1 wt.% Co_3O_4/CeO_2 to 2.5 $\mu mol_{N2O}\cdot s^{-1}\cdot nm^{-1}$ for 10 wt.% Co_3O_4/CeO_2. Thus, only in case of the cylindrical model, the size of the Co_3O_4 domains, derived from the TEM pictures (Figure 7a'-c'), allows for the regularization of the specific reactivity rates and their fairly good invariance with the Co_3O_4 loading implies that it can be regarded as circumferential turnover frequency.

The revealed regularization of the specific activity related to the interface length accounts for the strong dispersion effect of cobalt spinel active phase spread over ceria for the catalytic N_2O decomposition. In relation to the influence of the dispersion of cobalt spinel

nanoparticles on the deN_2O reactivity, an important role of the average distance between active centres located on cobalt spinel and those on ceria support can be pointed out. The redox properties of the cobalt centers would be in this case responsible for the activation of N_2O molecules and formation of atomic oxygen. The ceria support, in turn, would be responsible for the enhanced diffusion and recombination of oxygen, closing the catalytic cycle. It should be noted however, that in the case of large spinel domains the surface oxygen intermediates, formed in their central part, most probably recombine before reaching the Co_3O_4/CeO_2 interface region and are excluded from the beneficial two-phase mechanism. This explains why the cylindrical model is more adequate than the semi-spherical one.

Conclusions

A series of ceria supported cobalt spinel with 1-20 wt.% loading catalysts was thoroughly characterized by XRD, XRF, XPS, TEM/EDX/EELS, RS, TPR, BET techniques and investigated in the catalytic decomposition of nitrous oxide. A strong dispersion effect on the catalyst turnover rate was observed and associated with a specific morphology of the spinel active phase due to progressive agglomeration of the Co_3O_4 nanocrystalites into compact domains with the increasing cobalt loading. A simple topological model of the Co_3O_4/CeO_2 interface periphery was proposed for regularization of the observed specific reactivity rates. The cylindrical shape of Co_3O_4 domains where used to normalize the deN_2O reaction rate with respect to the cobalt content and the length of the Co_3O_4/CeO_2 interface periphery. A fairly good invariance of such reactivity parameter with the Co_3O_4 loading indicates that it can be regarded as circumferential turnover frequency. It implies a two-step mechanism operating at the interface, where the redox properties of the cobalt component is responsible for the dissociation of N_2O molecules and formation of oxygen intermediates, whereas the ceria periphery is responsible for the enhanced diffusion and recombination of oxygen adspecies, closing the catalytic cycle.

Acknowledgments

The authors would like to acknowledge the Polish National Centre for Research and Development funding awarded by the decision number PBS2/A5/38/2013.

On the Polish part the research was partially carried out with the equipment purchased thanks to the financial support of the European Regional Development Fund in the framework of the Polish Innovation Economy Operational Program (contract no. POIG.02.01.00-12-023/08).

Table captions

wt.% Co_3O_4*	XRF wt.% Co_3O_4[#]	Co/Ce*	XPS Co/Ce[#]	XPS wt.% Co_3O_4[#]	XPS $Ce^{3+}/(Ce^{3+}+Ce^{4+})$ x100 % (atomic)
0	-	-	-	-	33.4
1	1.5	0.02	0.02	0.7	34.9
5	5.9	0.11	0.03	1.4	35.0
10	10.4	0.24	0.05	2.1	36.4
20	16.7	0.54	0.13	5.9	37.3

Table 2

band	Binding energy/eV CeO_2	1 wt.% Co_3O_4 /CeO_2	5 wt.% Co_3O_4 /CeO_2	10 wt.% Co_3O_4 /CeO_2	20 wt.% Co_3O_4 /CeO_2
v_0	880.0	880.9	-	-	-
v	882.0	882.2	882.1	882.3	882.2
v'	883.9	884.1	883.4	883.7	883.6
v''	888.6	888.8	888.7	888.9	888.9
v'''	898.1	898.2	898.1	898.3	898.2
u_0	900.6	900.8	900.6	900.8	900.7
u'	902.1	902.6	901.9	902.6	902.1
u''	907.3	907.3	907.3	907.3	907.4
u'''	916.5	916.6	916.5	916.7	916.6

Table 3

wt.% Co_3O_4	N_2O conversion at 400 °C	r_{400}/µmol$_{N2O}$·g$_{Co3O4}^{-1}$·s^{-1}
0	0.04	-
1	0.22	8.18
5	0.24	1.78
10	0.43	1.60
20	0.38	0.71
100	0.44	0.16

Figure captions

Figure 1. XRD patterns of Co_3O_4/CeO_2 samples with different content of Co_3O_4; A – 20 wt.%Co_3O_4/CeO_2, B – 10 wt.%Co_3O_4/CeO_2, C – 5 wt.%Co_3O_4/CeO_2, D – 1 wt.%Co_3O_4/CeO_2, E – CeO_2.

Figure 2. Raman spectra of the Co_3O_4/CeO_2 catalysts with different content of Co_3O_4; A – 20 wt.%Co_3O_4/CeO_2, B – 10 wt.%Co_3O_4/CeO_2, C – 5 wt.%Co_3O_4/CeO_2, D – 1 wt.%Co_3O_4/CeO_2, E – CeO_2.

Figure 3. H_2-TPR profiles for the Co_3O_4/CeO_2 catalysts with different content of Co_3O_4; A – Co_3O_4, B – 10 wt.% Co_3O_4/CeO_2, C – 1 wt.% Co_3O_4/CeO_2.

Figure 4. XPS spectra of Co2p, region of Co_3O_4/CeO_2 catalysts; A – 20 wt.%Co_3O_4/CeO_2, B – 10 wt.%Co_3O_4/CeO_2, C – 5 wt.%Co_3O_4/CeO_2, D – 1 wt.%Co_3O_4/CeO_2.

Figure 5. XPS spectra of O1s, region of Co_3O_4/CeO_2 catalysts; A) 20 wt.%Co_3O_4/CeO_2, B) 10 wt.%Co_3O_4/CeO_2, C) 5 wt.%Co_3O_4/CeO_2, D) 1 wt.%Co_3O_4/CeO_2, E) CeO_2.

Figure 6. XPS spectra of Ce3d, region of Co_3O_4/CeO_2 catalysts; A – 20 wt.%Co_3O_4/CeO_2, B – 10 wt.%Co_3O_4/CeO_2, C – 5 wt.%Co_3O_4/CeO_2, D – 1 wt.%Co_3O_4/CeO_2, E – CeO_2.

Figure 7. Representative series of S/TEM images: Co_3O_4/CeO_2 with different Co_3O_4 loading equal to 1, 5, 10 wt.%, respectively together with HRTEM images. HAADF STEM images coupled with EDX elemental distribution of Co-Ka (red) (a-c), graphical overlay of the Co_3O_4(red)/CeO_2(orange) epitomizing samples differentiation in particles distribution and agglomeration (a'-c'). HRTEM images together with indicated crystal shapes overlays (d-d'), indexed Co_3O_4/CeO_2 FFT patterns (d-insert), EELS elemental map of the 10% Co_3O_4/CeO_2 at nanometer scale: color map overlaying background corrected absorption edges of Ce-$M_{4,5}$ (green), Co-$L_{2,3}$ (red), O-K (black) (d'-insert).

Figure 8. Conversion curves for N_2O decomposition reaction over the Co_3O_4/CeO_2 catalysts.

Figure 9. Catalytic activity in N_2O decomposition reaction represented by the conversion of N_2O and apparent reaction rate per gram of cobalt spinel with its concentration derived from

XRF – r_{XRF}, XPS – r_{XPS}, and apparent reaction rate per the interface Co_3O_4-CeO_2 peripheral length - r_{peri}, at 400 °C.

Figure 10. Conversion of N_2O at 400°C plotted against relative Ce^{3+} content.

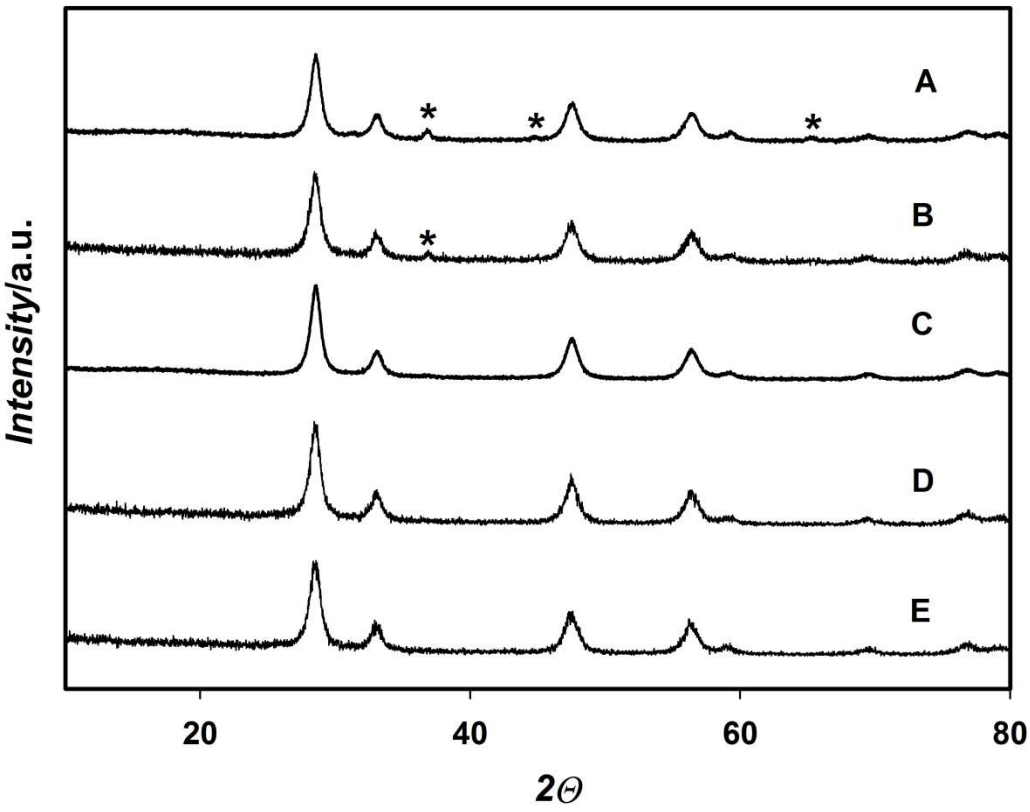

Figure 1

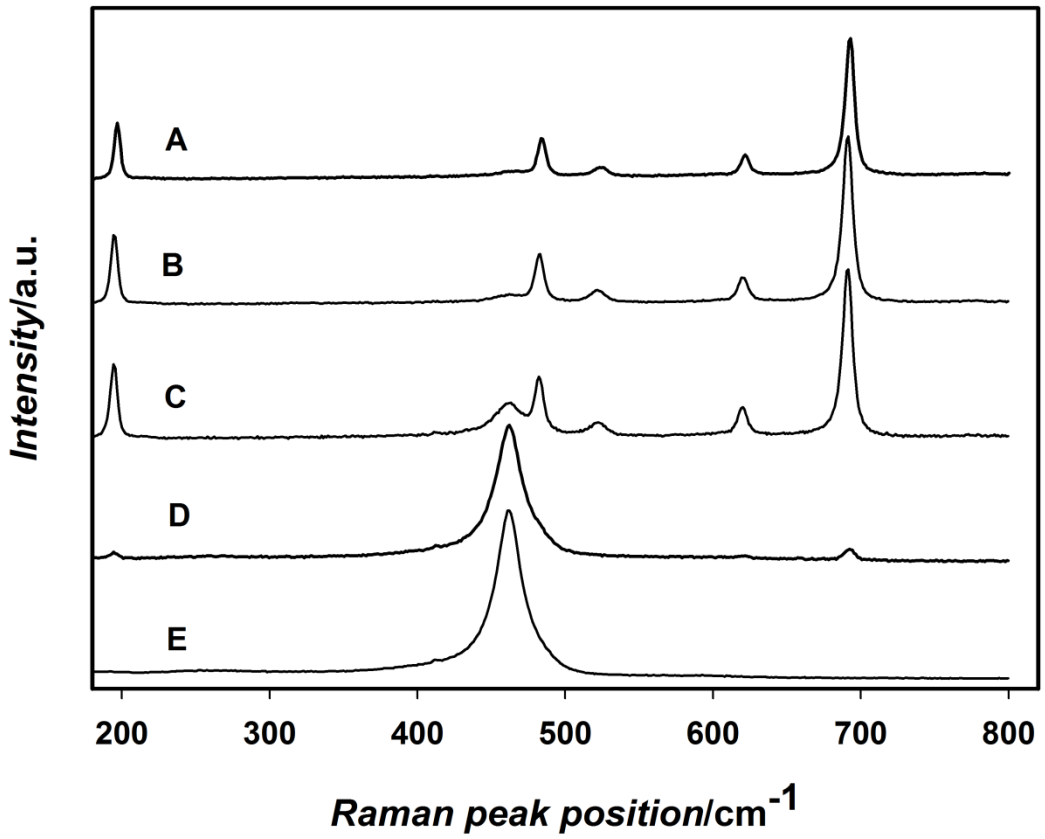

Figure 2

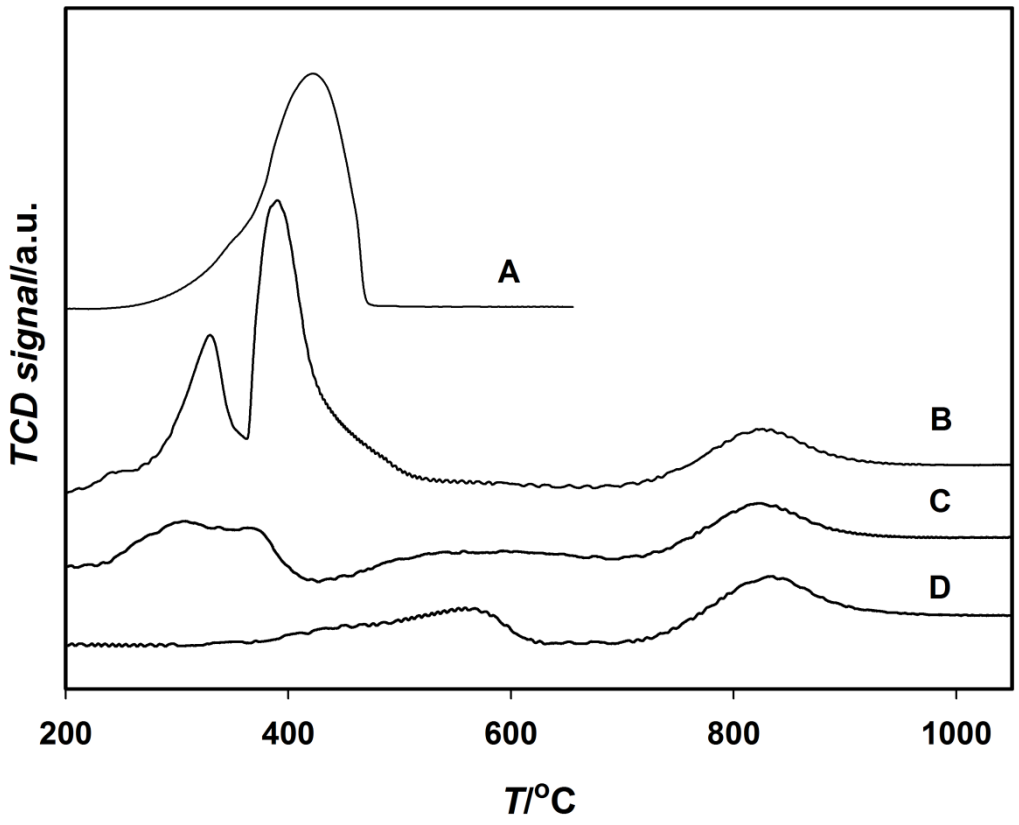

Figure 3

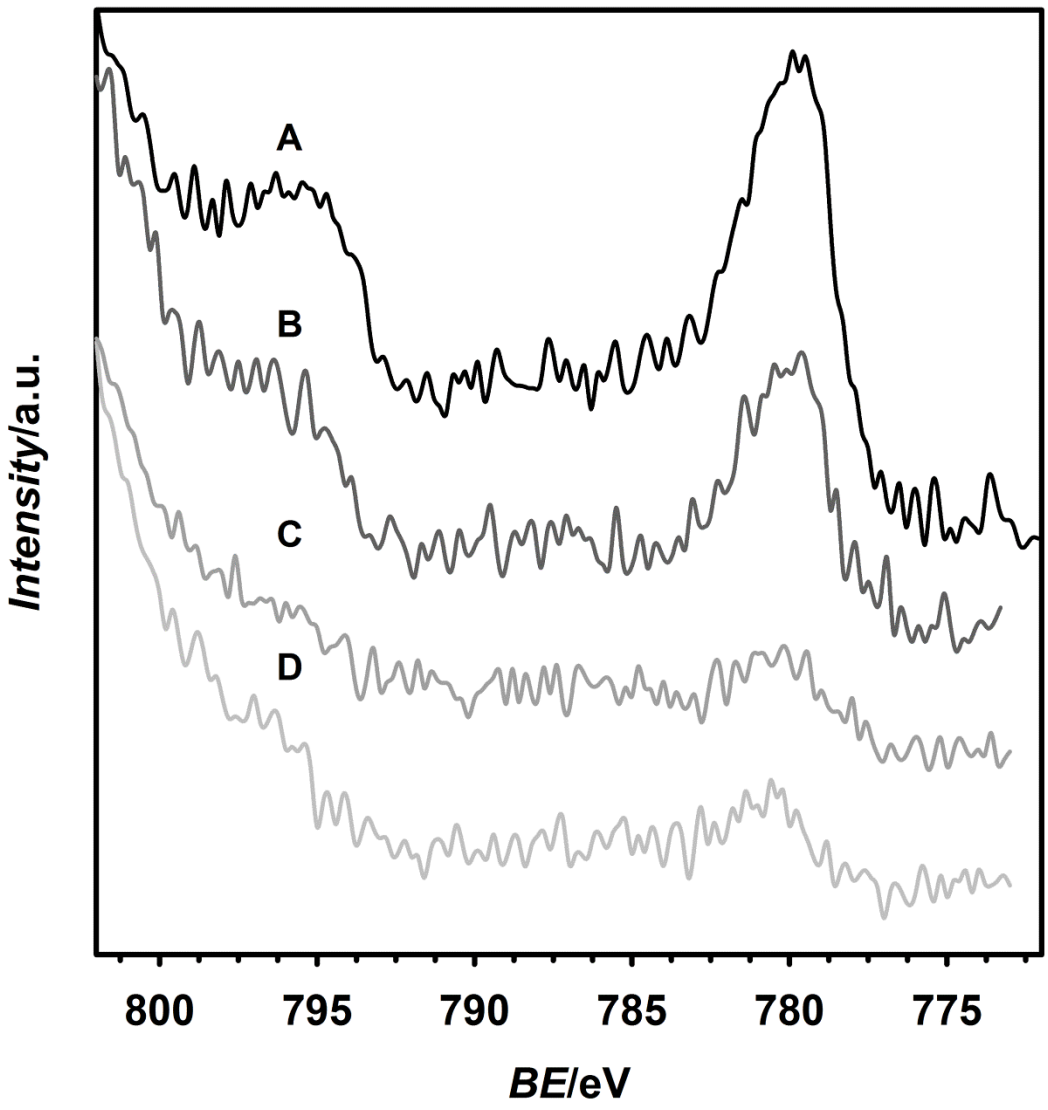

Figure 4

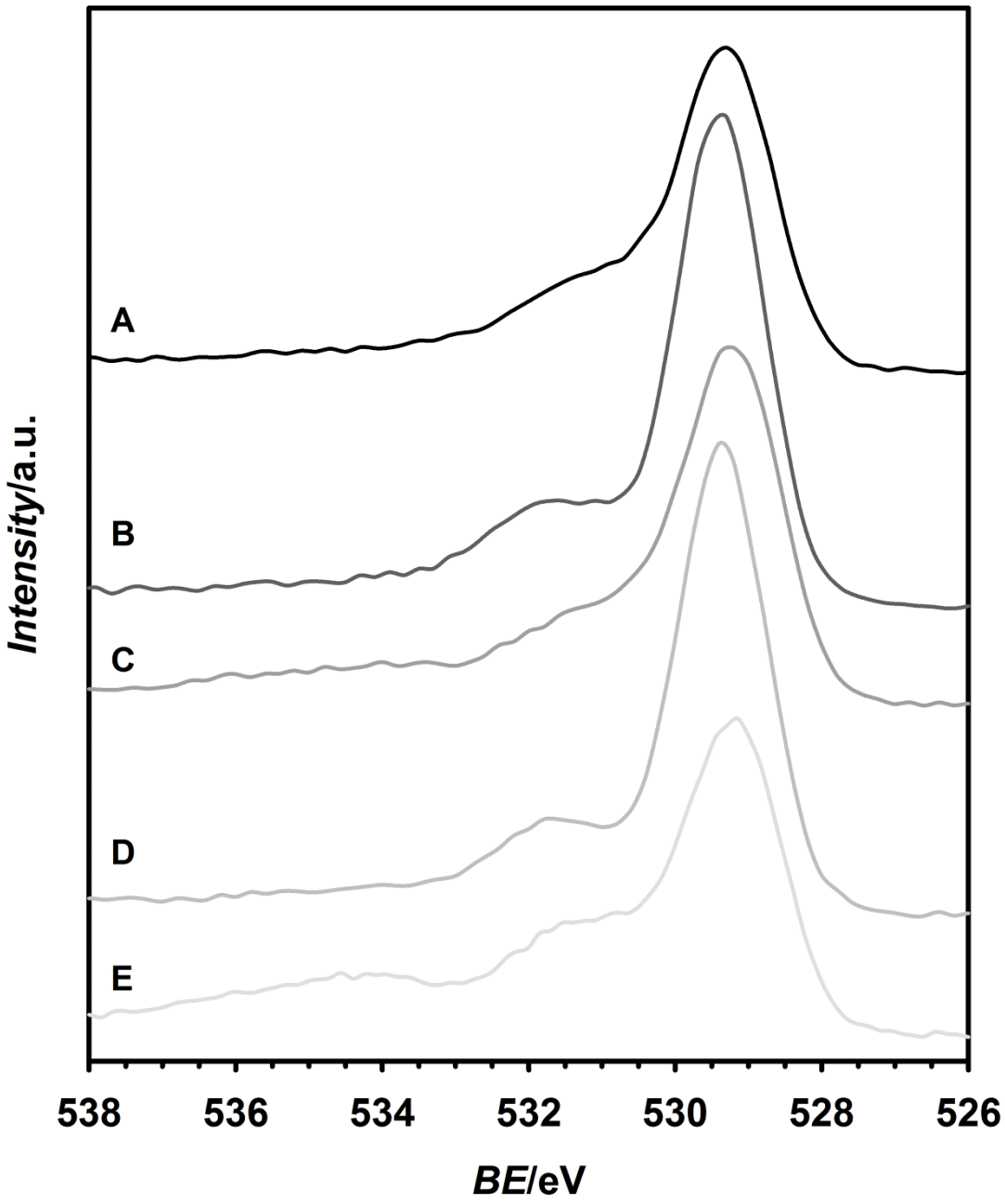

Figure 5

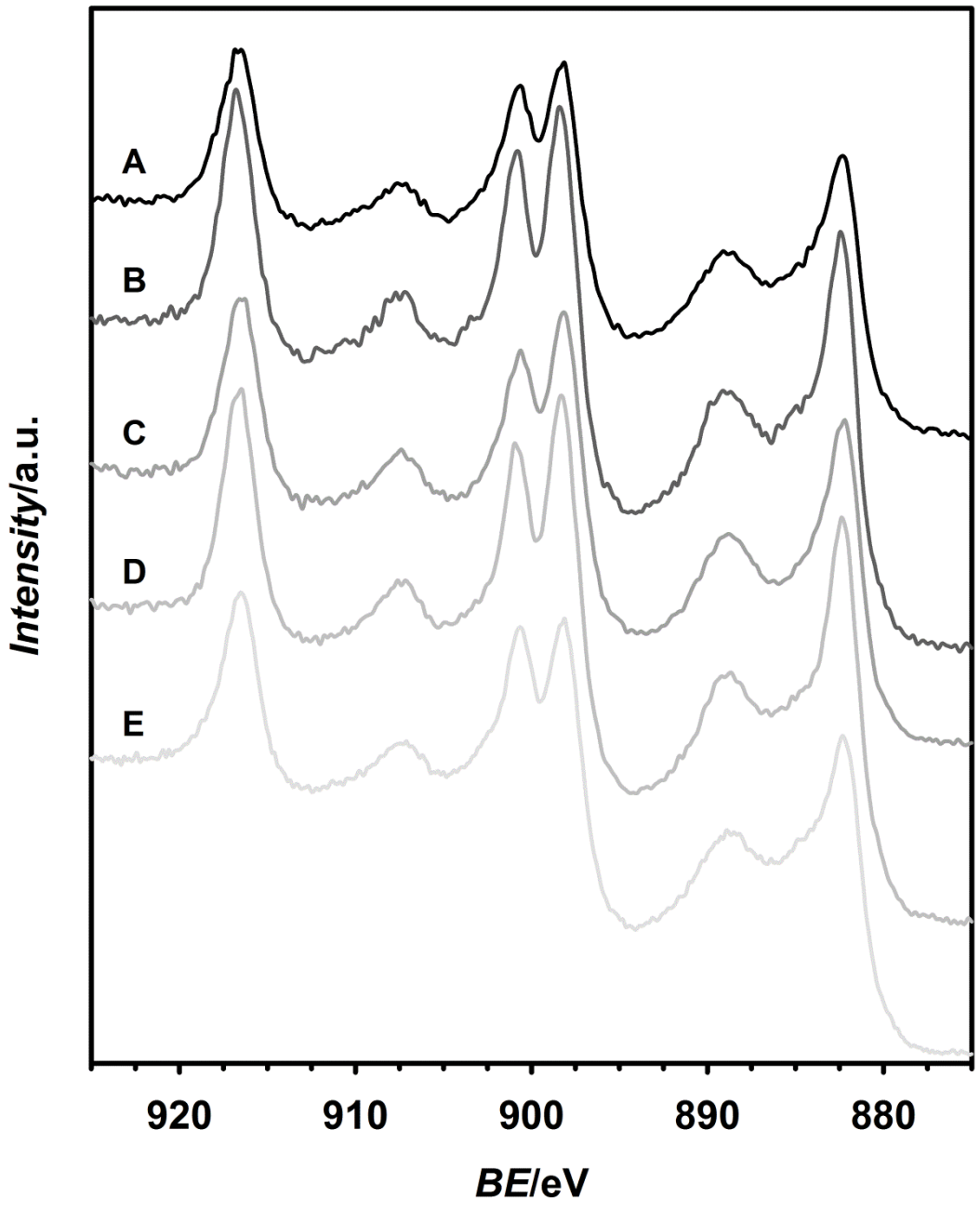

Figure 6

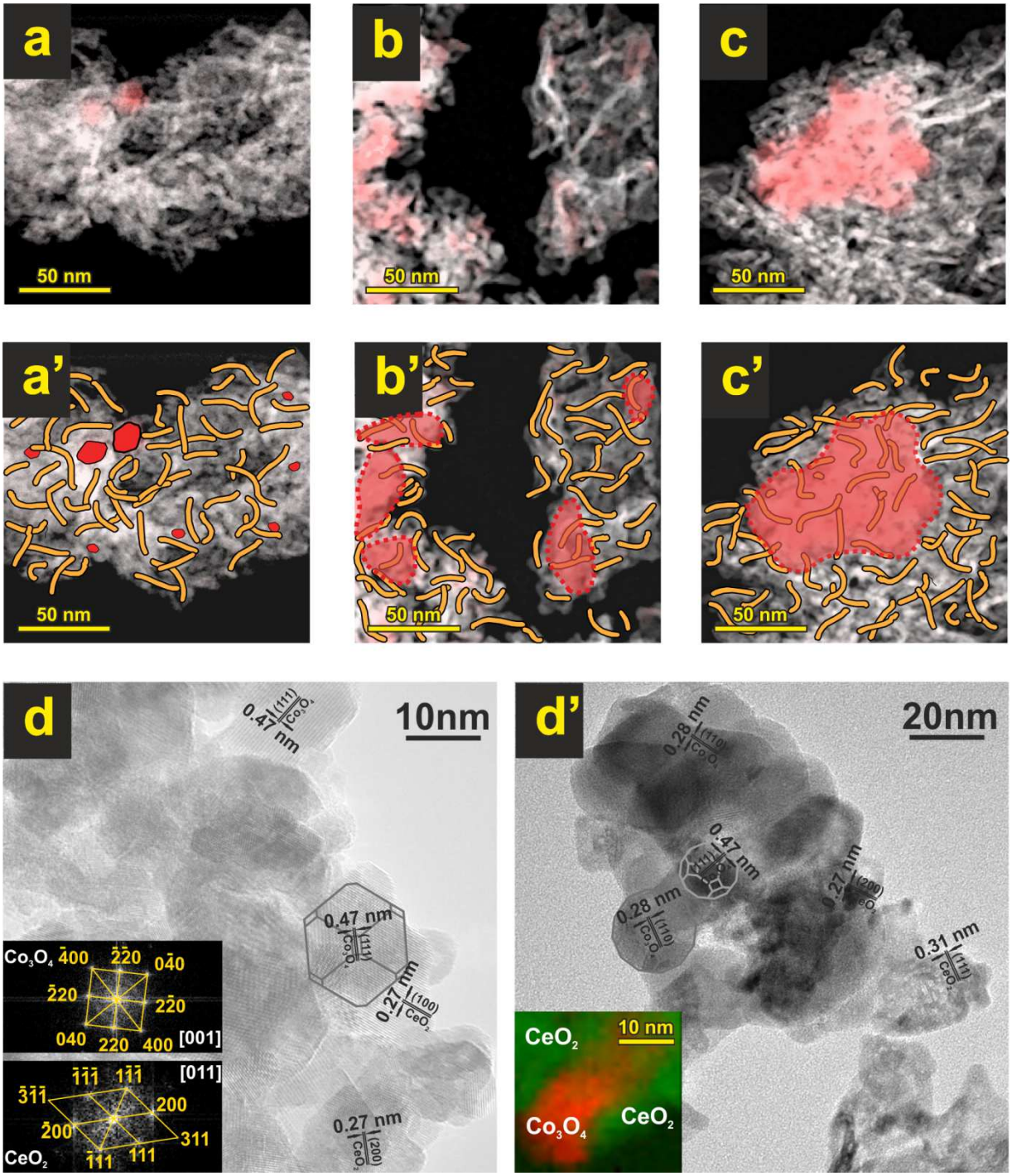

Figure 7

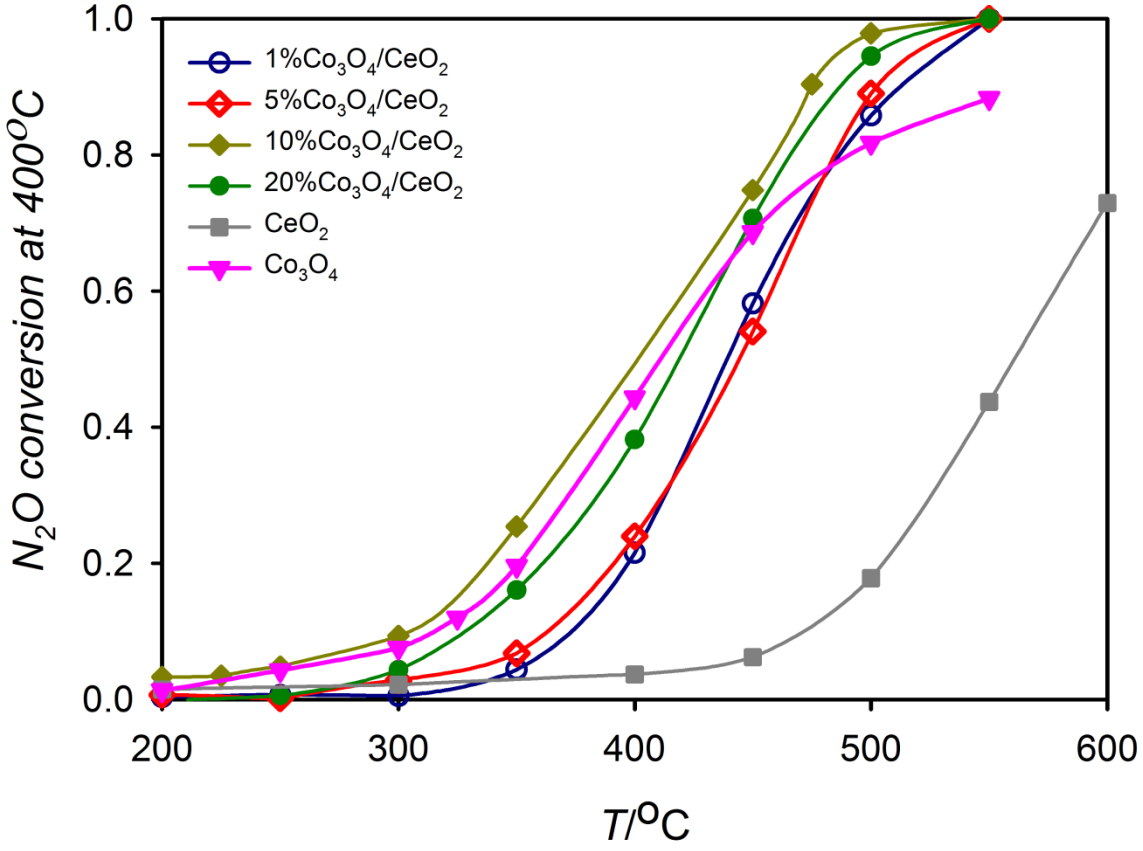

Figure 8

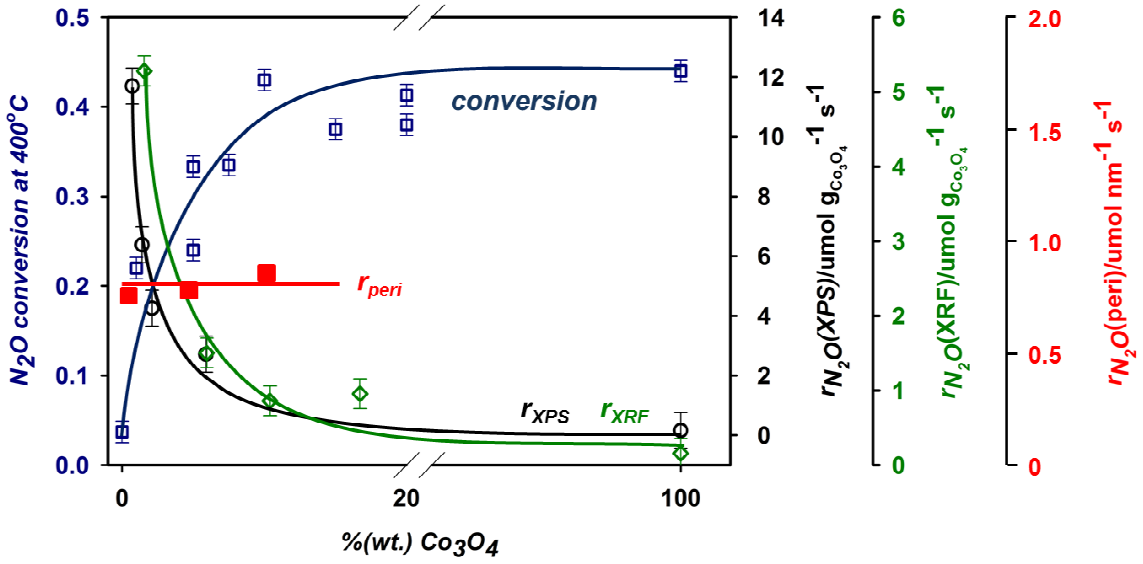

Figure 9

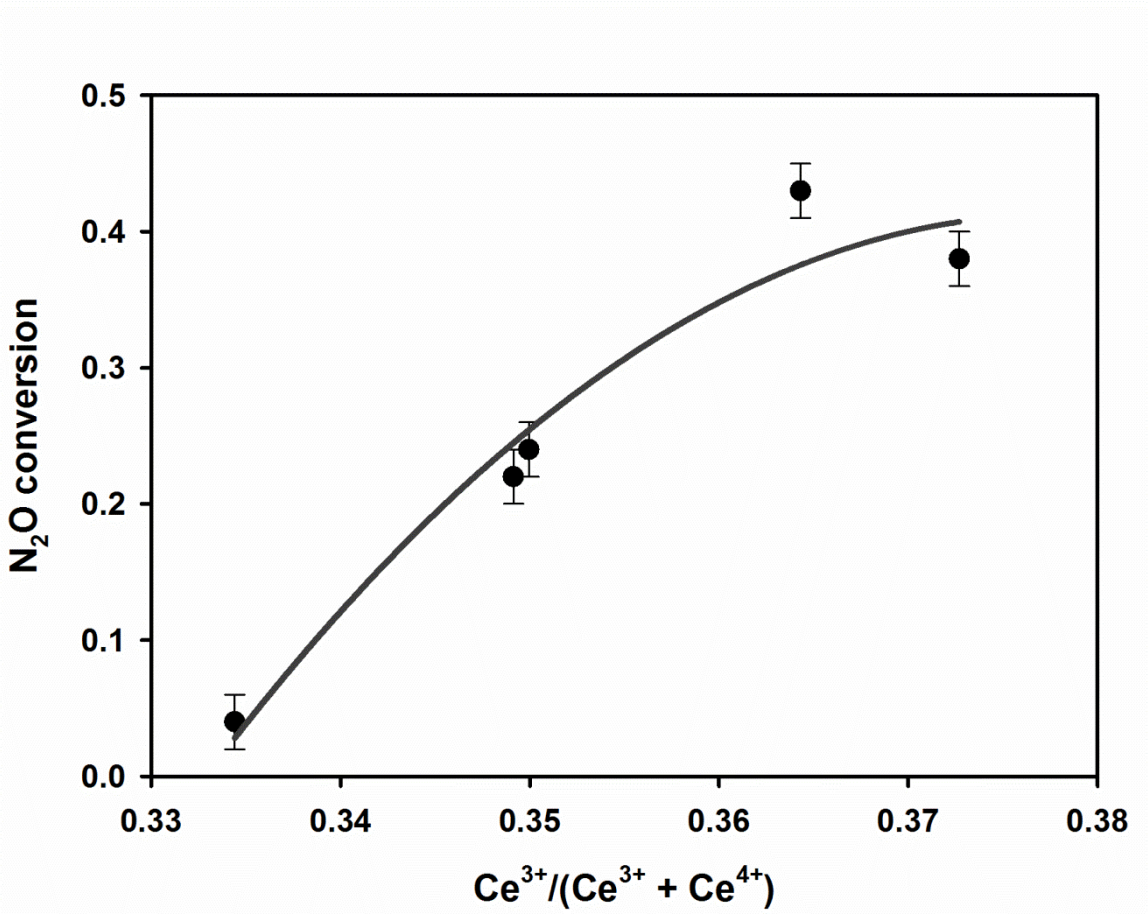

Figure 10

References

Table 1 Comparison of the surface (XPS) and bulk (XRF) content of cobalt oxide and the relative amount of Ce^{3+} in series of ceria supported cobalt catalysts. (*) theoretical and (#) experimental.

Table 2 XPS peak positions in the Ce 3d energy range obtained for the supported oxide samples and CeO_2.

Table 3 Kinetic parameters for N_2O decomposition over CeO_2 supported Co_3O_4 catalysts.

Table 1

[1] J. Pérez-Ramírez, F. Kapteijn, K. Schöffel, J.A. Moulijn, Appl.Catal. B 44 (2003) 117.

[2] E.V. Kondratenko, J. Pérez-Ramírez, Catal. Today 121 (2007) 197.

[3] S.J. Lee, I.S. Ryu, B.M. Kim, S.H. Moon, Int. J. Greenh. Gas Con. 5 (2011) 167.

[4] A. Szimizu, K. Tanaka, M. Fujimori, Chemosphere - Global Change Sci. 2 (2000) 425.

[5] J.P. Dacquin, C. Dujardin, P. Granger, J. Catal. 253 (2008) 37.

[6] S. Parres-Esclapez, M.J. Illán-Gómez, C.S.-M. de Lecea; A. Bueno-López, Appl. Catal,. B 96 (2010) 370.

[7] M. Hussain, D. Fino, N. Russo, J. Hazard. Mater. 211-212 (2012) 255.

[8] F. Kapteijn, J. Rodriguez-Mirasol, J.A. Moulijn, Appl. Catal. B 9 (1996) 25.

[9] J.P. Dacquin, C. Lancelot, C. Dujardin, P. Da Costa, G. Djega-Mariadassou, P. Beaunier, S. Kaliaguine, S. Vaudreuil, S. Royer, P. Grange, Appl. Catal., B 91 (2009) 596.

[10] B.M. Abu-Zied, S.A. Soliman, S.E. Abdellah, J. Ind. Eng. Chem., 21 (2015) 814.

[11] S. Sklenak, P.C. Andrikopoulos, B. Boekfa, B. Jansang, J. Nováková, L. Benco, T. Bucko, J. Hafner, J. Dédecék, Z. Sobalík, J. Catal. 272 (2010) 262.

[12] L. Obalová, K. Karásková, K. Jirátová, F. Kovanda, Appl. Catal., B 90 (2009) 132.

[13] W.-S. Ju, M. Matsuoka, M.Anpo, Int. J. Photoenergy, 5 (2003) 17.

[14] L. Chmielarz, P. Kuśtrowski, M. Drozdek, M. Rutkowska, R. Dziembaj, M. Michalik, P. Cool, E.F. Vansant, J. Porous Mater. 18 (4) (2011) 483.

[15] M. Hussain, P. Akhter, D. Fino, N. Russo, J. Environ. Chem. Eng. 1(3) (2013) 164.

[16] R. Sundararajan, V. Srinivasan, Appl. Catal. 73 (1991) 165.

[17] N. Russo, D. Fino, G. Saracco, V. Specchia, Catal. Today 119 (2007) 228.

[18] L. Xue, C. Zhang, H. He, Y. Teraoka, Appl. Catal. B 75 (2007) 167.

[19] C. Ohnishi, K. Asano, S. Iwamoto, K. Chikama, M. Inoue, Studies in Surf. Sci. Catal. 162 (2006) 737.

[20] P. Stelmachowski, G. Maniak, J. Kaczmarczyk, F. Zasada, W. Piskorz, A. Kotarba, Z. Sojka, Appl. Catal., B 146 (2014) 105.

[21] L. Yan, T. Ren, X. Wang, Q. Gao, D. Ji, J. Suo, Catal. Commun. 4 (2003) 505.

[22] L. Yan, T. Ren, X. Wang, D. Ji, J. Suo, Appli. Catal. B 45 (2003) 85.

[23] G. Maniak, P. Stelmachowski, J.J. Stanek, A. Kotarba, Z. Sojka, Catal. Commun. 15 (2011) 127.

[24] M. Inger, P. Kowalik, M. Saramok, M. Wilk, P. Stelmachowski, G. Maniak, P. Granger, A. Kotarba, Z. Sojka, Catal. Today 176 (2011) 365.

[25] F. Zasada, P. Stelmachowski, G. Maniak, Jean-Francois Paul, A. Kotarba, Z. Sojka, Catal. Lett. 127 (2009) 126.

[26] P. Stelmachowski, G. Maniak, A. Kotarba , Z. Sojka, Catal. Commun. 10 (2009) 1062.

[27] G. Maniak, P. Stelmachowski, A. Kotarba, Z. Sojka, V. Rico-Pérez, A. Bueno-López, Appl. Catal. B 136– 137 (2013) 302.

[28] G. Grzybek, P. Stelmachowski, S. Gudyka, A. Duch, K. Ćmil, A. Kotarba, Z. Sojka, Appl. Catal. B 168-169 (2015) 509.

[29] V. Boissel, S. Tahir, C.A. Koh, Appl. Catal. B 64 (2006) 234.

[30] Q. Shen, L. Li, J. Li, H. Tian, Z. Hao, J Hazard Mater. 163 (2009) 1332.

[31] S.C. Christoforou, E.A. Efthimiadis, I.A. Vasalos, Catal. Lett. 79 (2002) 137.

[32] J. Oi, A. Obuchi, G.R. Bamwenda, A. Ogata, H. Yagita, S. Kushiyama, K. Mizuno, Appl. Catal. B 12 (1997) 277.

[33] A. Bueno-Lopez, I. Such-Basanez, C. Salinas-Martinez de Lecea, J. Catal. 244 (2006) 102.

[34] P.S.S. Reddy, N. Seshu Babu, N. Pasha, N. Lingaiah, P.S. Sai Prasad, Catal. Commun. 9 (2008) 2303.

[35] J. Yang, L. Lukashuk, J. Akbarzadeh, M. Stöger-Pollach, H. Peterlik, K. Föttinger, G. Rupprechter, U. Schubert, Chem. Eur. J. 21 (2015) 885.

[36]. S. Parres-Esclapez, I. Such-Basañez, M.J. Illán-Gómez, C. Salinas-Martínez de Lecea,

A. Bueno-López, J. Catal. 276 (2010) 390.

[37] M. Inger, M. Wilk, M. Saramok, G. Grzybek, A. Grodzka, P. Stelmachowski, W. Makowski, A. Kotarba, Z. Sojka, Ind. Eng. Chem. Res., 53 (2014) 10335.

[38] I.I. Soykal, B. Bayram, H. Sohn, P. Gawade, J.T. Miller, U.S. Ozkan, Appl. Catal. A 449 (2006) 47.

[39] Y. Sato, Y. Soma, T. Miyao, S. Naito, Appl. Catal. A 304 (2006) 78.

[40] L.N. Ikryannikova, A.A. Aksenov, G.L. Markaryan, G.P. Muraveva, B.G. Kostyuk,

A.N. Kharlanov, E.V. Lunina, Appl. Catal. A 210 (2001) 225.

[41] W.H. Weber, K.C. Hass, J.R. McBride, Phys. Rev. B 48 (1993) 178.

[42] Y. Wei, K.W. Nam, K.B. Kim, G. Chen, Solid State Ionics 177 (2006) 29.

[43] L.V. Gasparov, D.B. Tanner, D.B. Romero, H. Berger, G. Margaritondo, L. Forro, Phys. Rev. B 62 (2000) 7939.

[44] Z.H. Zhou, J.M. Xue, J. Wang, H.S.O. Chan, T. Yu, Z.X. Shen, J. Appl. Phys. 91 (2002) 6015.

[45] R. Dziembaj, M. Zaitz, M. Rutkowska, M. Molenda, L. Chmielarz, Catal. Today 191 (2012) 121.

[46] S. Parres-Esclapez, M.J. Illan-Gomez, C. Salinas-Martinez de Lecea, A. Bueno-Lopez, Appl. Catal. B 96 (2010) 370.

[47] M. Sun, L. Wang, B. Feng, Z. Zhang, G. Lu, Y. Guo, Catal. Today 175 (2011) 100.

[48] J.L. Gautier, E. Rios, M. Gracia, J.F. Marco, J.R. Gancedo, Thin Solid Films 311 (1997) 51.

[49] A. Laachir, V. Perrichon, A. Badri, J. Lamotte, E. Catherine, J.–C. Lavalley, J. El Fallah, L. Hilaire, F. le Normand, E. Quéméré, G. Noël Sauvion, O. Touret, J. Chem. Soc. Faraday Trans. 87 (1991) 1601.

[50] H.A.E. Hagelin-Weaver, G.B. Hoflund, D.M. Minahan, G.N. Salaita, Appl. Surf. Sci. 235 (2004) 420.

[51] M.M. Natile, A. Glisenti, Chem. Mater. 17 (2005) 3403.

[52] L. Xue, Ch. Zhang, H. He, Y. Teraoka, Appl. Catal. B 75 (2007) 167.

[53] F. Zasada, J. Gryboś , P. Indyka , W. Piskorz , J. Kaczmarczyk , Z. Sojka, J. Phys. Chem. C 118 (2014) 19085.

[54] S. Turner, S. Lazar, B. Freitag, R. Egoavil, J. Verbeeck, S. Put, Y. Strauven, G. Van Tendeloo, Nanoscale 3 (2011) 3385.